Article

Future climate-driven fires may boost ocean productivity in the iron-limited North Atlantic
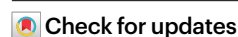
Elisa Bergas-Masso [1,2] ✉, Douglas S. Hamilton [3], Stelios Myriokefalitakis [4], Sagar Rathod[5,6,7], María Gonçalves Ageitos [1,2,9] & Carlos Pérez García-Pando [1,8,9]

Rapid shifts in fire regimes affect the carbon cycle by releasing carbon and nutrients such as iron (Fe), potentially enhancing marine productivity and carbon export. Here we use fire emission projections and Earth system models to examine how climate-driven changes in fire emissions may alter soluble Fe (SFe) deposition and productivity. By century's end, climate change could increase Fe emissions from fires by 1.7–1.8 times beyond projections considering only direct human influences. Model projections show rising SFe deposition in Northern Hemisphere high latitudes under increasing socio-economic activity, potentially boosting the impact of SFe deposition on productivity in the Fe-limited North Atlantic by up to 20% annually (40% in summer), assuming stable macronutrient levels. However, declining macronutrient availability may shrink Fe-limited areas, where climate-driven fires could offset productivity losses by 7–8%. In the Southern Ocean, fossil fuel emissions primarily control SFe deposition, as reductions in anthropogenic fires counterbalance climate-driven increases.

Wildfires are a crucial component of the Earth system, connecting the biosphere, hydrosphere, lithosphere, cryosphere and atmosphere. They affect vegetation structure; alter the energy, water, carbon and biogeochemical cycles; and change the composition of the atmosphere, which impacts the quality of the air and water[1–5]. Although often viewed as carbon sources[6], fires play essential ecological roles and can even enhance carbon capture through regrowth and nutrient cycling[2,7]. Downwind, fires supply nutrients, including soluble (bioavailable) iron (SFe), nitrogen and phosphorus, which can stimulate marine productivity[8–10], potentially impacting carbon export.

Recent shifts in fire regimes reflect the complex interplay of climate change, human land use and ecosystem dynamics[11,12]. Over the past two decades, global burned area has declined by ~25%, mainly due to the conversion of natural grasslands to agriculture, particularly in African savannahs[13,14]. However, wildfire frequency and severity have increased, especially at mid-to-high latitudes[15–20], due to changes in climate. Consequently, global fire emissions have remained relatively constant[19]. In this context, understanding future fires' potential influence on marine biogeochemistry—particularly through SFe deposition, which can stimulate phytoplankton growth in Fe-limited areas—is of growing interest[21,22]. Projections of future fire impacts, however, remain

[1]Barcelona Supercomputing Center, Barcelona, Spain. [2]Universitat Politècnica de Catalunya, Barcelona, Spain. [3]Department of Marine, Earth and Atmospheric Sciences, North Carolina State University, Raleigh, NC, USA. [4]Institute for Environmental Research and Sustainable Development, National Observatory of Athens, Athens, Greece. [5]La Follette School of Public Affairs, University of Wisconsin–Madison, Madison, WI, USA. [6]Nelson Institute Center for Sustainability and the Global Environment, University of Wisconsin–Madison, Madison, WI, USA. [7]Office of Sustainability, University of Wisconsin–Madison, Madison, WI, USA. [8]Catalan Institution for Research and Advanced Studies, Barcelona, Spain. [9]These authors contributed equally: María Gonçalves Ageitos, Carlos Pérez García-Pando. ✉e-mail: elisa.bergas@bsc.es

uncertain due to limited understanding of the interactions between human influence, climate and fire dynamics[23,24].

Recent studies of extreme fires highlight their potential impact on ocean productivity. The 2019–2020 Australian fires led to phytoplankton blooms far exceeding the climatological mean in downwind regions[25–28]. Similarly, intense Siberian fires have been shown to increase SFe deposition in the Pacific Ocean[29]. Fires can be a more important source of SFe than dust[9,30], as fire Fe dissolves more readily in the atmosphere due to acidic and organic compounds in smoke plumes[30–32]. As it reaches Fe-limited areas distant from the primary dust sources, Fe from fires may contribute to higher carbon export efficiency than Fe from lithogenic sources[21,33].

Fe-limited ocean regions, spanning the subpolar North Pacific, the Southern Ocean, the eastern equatorial Pacific and the summer high-latitude North Atlantic, make up one third of the global ocean[34–36]. Even small increases in SFe deposition in these high-nutrient, low-chlorophyll (HNLC) regions can boost productivity, alter community composition and enhance carbon sequestration[35,36]. The high-latitude North Atlantic and Southern Ocean are particularly efficient at carbon uptake and long-term organic carbon storage[37–40], making any shifts in SFe flux to these areas especially impactful.

Assessing the impact of future fire regimes on ocean health requires a global climate modelling framework. The Shared Socio-economic Pathway (SSP) scenarios from the Sixth Coupled Model Intercomparison Project (CMIP6) offer fire emission projections linked to human activities, but they disregard climate-driven changes in natural fire activity[41]. Fire-enabled vegetation models within Earth system models (ESMs) can address this gap by simulating fire dynamics on the basis of factors such as temperature and precipitation. By combining SSP data with these ESM projections, fire scenarios shaped by both socio-economic and climate change influences can be better understood[42].

This study leverages new twenty-first-century fire emission projections[42] (Methods) to assess how combined anthropogenic and climate-driven factors affect future Fe emissions from fires and atmospheric SFe deposition to the global ocean. We employ two ESMs with advanced Fe aerosol cycle modules (EC-Earth3-Iron[32] and CAM6-MIMI[43]) (Methods) across three CMIP6 SSP scenarios, SSP1-2.6 (SSP126), SSP3-7.0 (SSP370) and SSP5-8.5 (SSP585), which span a range of mitigation and emission trajectories (Methods). Our analysis first isolates the future effects of these previously unaccounted Fe emissions from climate-driven fire changes relative to changes in other Fe sources across scenarios using atmosphere-only simulations. It also examines how future climate conditions may additionally alter SFe deposition by impacting atmospheric Fe dissolution and deposition dynamics (Methods). We demonstrate potential substantial increases in future Fe emissions from climate-driven fires in the northern high latitudes. Key oceanic regions highly susceptible to these changes are identified by estimating changes in the impact of SFe on marine productivity (Methods), with the high-latitude North Atlantic emerging as an area notably affected. The study's framework also assesses which factors, either current Fe cycle uncertainties or policy efficacy, most affect SFe deposition over HNLC regions. This allows us to highlight the importance of comprehensive, interdisciplinary approaches in climate impact assessments with the final aim of better informing CMIP efforts and future policy.

Impact of climate-driven fires on future atmospheric iron

Fire Fe emissions are subject to the episodic and unpredictable nature of fires, which complicates obtaining globally representative aerosol samples for analysing smoke plume composition and atmospheric transport pathways[26]. Modelling can help fill this gap by using estimates from available observational studies that link Fe emissions to

co-emitted species such as black carbon (BC) and organic carbon (OC) aerosols[44].

Using two different ESMs and present-day emissions from the CMIP6 historical inventory, which uses the Global Fire Emissions Database version 4.1s (GFED4s)[45] (Methods), we obtained a mean present-day (~2010 CE) global fire Fe emission of 0.76 (range, 0.57–0.94) Tg Fe yr^{-1}. These estimates align with recent modelling studies, which report values from 0.52 to 2.2 Tg Fe yr^{-1} (ref. 46). Fire Fe emissions are mainly concentrated in vegetated regions from 45° S to 75° N, with tropical peaks near 10° N and 10° S (Supplementary Fig. 1). The northern peak is related to grassland fires, while the southern peak is driven by grassland fires and deforestation in South America and Indonesia. A secondary peak, around 55° N, corresponds to boreal fires.

For future estimates, we used an emission dataset that accounts for fire scenarios influenced by both socio-economic and climate factors[42]. This dataset integrates information from an ensemble of six ESMs within the CMIP6 framework, which simulate interactive fires in response to changes in climate and vegetation, combined with SSP emission data[42]. The projections are then bias-corrected using present-day GFED4s estimates[42] (Methods). Additionally, we conducted simulations using the standard SSP fire emission projections (Supplementary Fig. 2), enabling us to isolate climate-driven changes in fires from those driven by anthropogenic factors (Methods). Anthropogenic fire changes in our methodology are attributed to human activities such as land-use changes, management and accidents, which are driven by economic and demographic factors[13,47]. In contrast, climate-driven fire changes arise from fire-favourable conditions such as low humidity and high temperatures, primarily influenced by anthropogenic climate change.

Climate drivers enhance global future fire Fe emissions, leading to increases of 1.7 to 1.8 times above CMIP6-SSP standard projections across all scenarios. Without these drivers, even the most extreme scenarios (SSP370 and SSP585) would yield fire Fe emissions below present-day levels.

Our projections indicate a substantial increase in fire Fe emissions across the extra-tropics by the century's end, consistent across all socio-economic scenarios. The highest increases appear in scenarios with limited climate mitigation and high radiative forcing (SSP370 and SSP585) (Methods). Under SSP585, for example, emissions may reach levels three times present-day levels in some latitudinal bands. This rise is more pronounced in the Northern Hemisphere (NH) than in the Southern Hemisphere (SH) due to the limited extra-tropical land area in the SH (Fig. 1). The steep rise in high-latitude emissions is largely climate-driven, with peak increases occurring during NH summers (Supplementary Fig. 3). In these latitudes, lightning-induced (climate-driven) fires are expected to remain dominant[48–50]. The extraordinary fire season in Canada in 2023 exemplifies the large and severe fires that lightning can trigger in these regions[6,51].

In tropical regions, especially in Africa, recent declines in fire emissions are primarily due to human activities such as converting grasslands to agricultural and pastoral land[13]. Future shifts in fire emissions will vary widely across socio-economic scenarios: SSP126, a sustainable, low-intervention pathway, shows decreases in anthropogenic-driven fires across all latitudes, while SSP370 and SSP585 show regional increases in the NH extra-tropical regions. SSP126's minimal climate impact contrasts with SSP370 and SSP585, which project moderate to high climate forcing combined with varying levels of human intervention (Methods). As a result, global fire Fe emission trends diverge, with SSP126 indicating a slight decline, and SSP370 and SSP585 showing increases up to 1.4 times above present-day levels.

Changes in fire Fe emissions lead to corresponding shifts in fire SFe deposition downwind. During atmospheric transport, Fe aerosols undergo chemical transformations, transitioning from insoluble to soluble forms that marine biota can use as micronutrients. The primary solubilization pathways are acidic and organic ligand-promoted
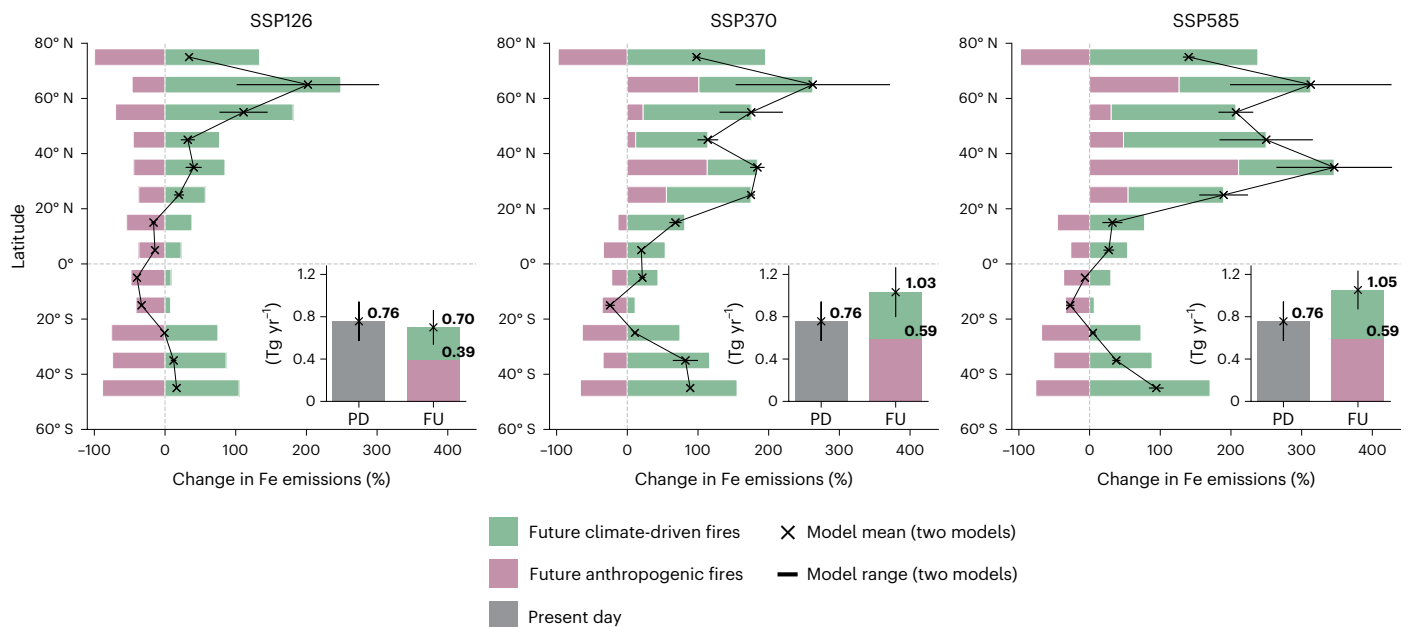
Fig. 1 | Future changes in fire iron emissions. Model-derived changes in fire iron emissions relative to present-day estimates by 10° latitude bands for each scenario (SSP126 (left), SSP370 (middle) and SSP585 (right)) are shown in black. The black crosses show the mean of the two models (EC-Earth3-Iron and CAM6-MIMI), and the black horizontal lines indicate the range between them. Purple bars denote the contribution of anthropogenic fires to future changes, while green bars illustrate the influence of climate-driven fires. The bar plots in the lower-right corners display global fire iron emission budgets (in Tg yr⁻¹) for the present day (grey) and end-of-century projections for each SSP, with contributions from anthropogenic and climate-driven fires shown in purple and green, respectively. The black crosses and lines again indicate the mean and range between the two models. PD, present day; FU, future.

dissolution, which are represented in the employed ESMs (Methods). Fire plumes, rich in acids[52] and organics[53], thereby facilitate the dissolution of Fe in the atmosphere.

The global fire SFe deposition and its attribution to climate versus anthropogenic factors mirror the patterns seen in fire Fe emissions (Supplementary Figs. 4 and 5). Maximum global fire SFe deposition occurs near the Equator, primarily in the Atlantic basin downwind of African fire sources, which are mainly anthropogenic. Climate-driven fires markedly affect NH fire SFe deposition (over 60%), particularly from North American boreal regions impacting the Arctic Ocean and North Atlantic (Fig. 2). Incorporating climate-driven effects on fire emissions results in lower Fe estimates than projections without these factors in only a limited number of regions (shown in pink in Fig. 2). In these areas, fire emissions are suppressed by climatic conditions, such as increased soil moisture, higher precipitation or reduced wind speed.

Iron deposition changes shaped by fires and fossil fuels

We have emphasized the importance of incorporating climate-driven fire changes in future fire Fe emission estimates, particularly in the high latitudes. However, to fully assess how future fires will impact SFe deposition in the ocean, it is crucial to consider concurrent changes in other sources of Fe influenced by socio-economic pathways. Our simulation distinguishes between changes in SFe deposition from fires and the SSP projected changes in fossil fuel emission sources (Methods).

Fires contribute over 30% of SFe deposition across various regions, regardless of the SSP scenario. Key areas affected include the Arctic, North Atlantic, equatorial Atlantic and Pacific, and southern Indian Ocean (Fig. 2). Fires in the Arctic and high-latitude North Atlantic contribute up to 70% of the total deposition, with regions such as the Beaufort Sea and Hudson Bay reaching the upper end of this range. This dominance results from minimal dust and fossil fuel contributions. In the SH, fire SFe contributes between 20% and 50% to the total SFe deposition in the Atlantic, influenced by southern African biomass burning. The impact of SFe from fires is also notable in the equatorial Pacific,

where biomass burning in Central and South America contributes 20–30%. While climate-driven fires dominate the fire contribution in the NH, anthropogenic fires primarily affect the SH regions.

Changes in SFe deposition between future and present-day levels exhibit considerable variability depending on the scenario (Fig. 3). Under SSP126, a reduction in SFe deposition is observed below 60° N, due to decreased anthropogenic activities affecting both fire and other anthropogenic aerosol emissions. Above 60° N, no discernible change occurs, as increased climate-driven fires offset reductions in fossil fuel emissions. SSP370 shows a global rise in SFe deposition, especially in equatorial regions and NH high latitudes, with mean latitudinal increases of up to 40%. The increment in equatorial SFe deposition is driven by both fossil fuel and fire aerosol Fe increases. In the NH high latitudes, the escalation stems from heightened anthropogenic (~10% increase) and climate-driven fires (~30% increase), reflecting the high population growth in this scenario. SSP585 shows a reduction in SFe deposition below 60° N, though smaller than under SSP126, due to decreases in non-fire anthropogenic emissions. Above 60° N, both anthropogenic and climate-driven fire increases outweigh the effects of non-fire aerosol reductions, leading to a 40% rise in SFe deposition under certain latitudinal bands. There are regional variations, with more pronounced increases downwind of North American boreal fires for the three scenarios. However, Eurasian boreal fires do not show such a strong signal. This disparity is due to differences in fire regimes[54] and the lower baseline SFe deposition rates downwind of North American boreal regions[32,55], making them more sensitive to changes in aerosol deposition.

In addition to emissions changes, climate-driven shifts in meteorological conditions may further influence SFe deposition from all Fe sources. We assessed this sensitivity using EC-Earth3-Iron (Methods), and our results (Supplementary Fig. 6) show that under high-mitigation scenarios (SSP126), projected changes remain similar to those under present-day meteorology. However, for SSP370 and SSP585, SFe deposition increases up to 100% higher than present-day levels in equatorial and tropical regions, with smaller increases in high latitudes.
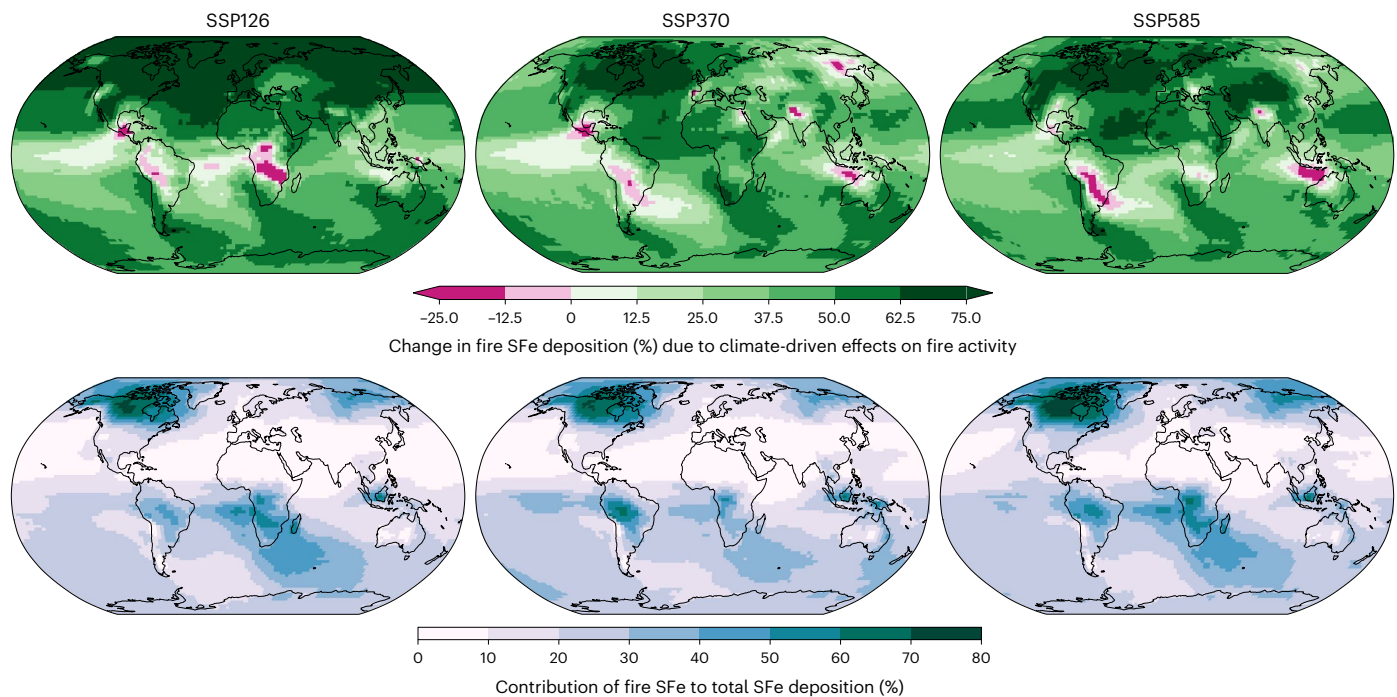
Fig. 2 | Contribution of climate-driven and anthropogenic-driven fires to SFe deposition. The top row shows how climate-driven effects on fire emissions impact SFe deposition from fires as per cent change. The bottom row shows the percentage of SFe deposition originating from fires considering all other sources. Fields are shown for future scenarios (SSP126, SSP370 and SSP585, from left to right). All fields shown represent the mean of two models (CAM6-MIMI and EC-Earth3-Iron).

This rise is associated with increases in water content and warmer temperatures[56,57], which, together with high atmospheric acidity, enhance solubilization and result in greater SFe deposition[46].

Impacts on Fe-limited oceans

Projected changes in SFe deposition are likely to impact Fe-limited HNLC ocean regions, where nitrogen and other nutrients are abundant, and light conditions during certain seasons support marine productivity, but Fe remains scarce[34,35,58]. Studies from Fe fertilization experiments, ocean surveys and modelling confirm that Fe supports phytoplankton growth, impacting net primary productivity (NPP)—the rate of photosynthetic carbon fixation minus the carbon used for respiration by autotrophic microbes—and, consequently, carbon export to the deep ocean.

We estimated the impact of our new future fire projections on NPP by calculating the portion specifically attributable to SFe deposition, denoted as NPP_{iron}. To quantify NPP_{iron}, we applied a range of carbon-to-SFe (C/SFe) ratios derived from experimental data in Fe-limited ocean regions[59,60]. Additionally, following previous studies[61], we defined Fe-limited regions on the basis of varying surface nitrate concentration thresholds[62] (Extended Data Fig. 1 and Methods).

Figure 4 shows present-day NPP_{iron} estimates in four Fe-limited regions (that is, the Southern Ocean, the equatorial Pacific, the North Pacific and the high-latitude North Atlantic) and projected end-of-century changes across scenarios, assuming present-day surface nitrate levels. The Southern Ocean and North Pacific display higher NPP_{iron} estimates than the equatorial Pacific and North Atlantic, due to the larger area of the former and the higher SFe deposition rates in the latter.

Under SSP126, a 17–46% reduction in NPP_{iron} is projected across all Fe-limited regions, primarily due to decreased fossil fuel emissions and reduced anthropogenic SFe from fires reaching the equatorial Pacific. Conversely, SSP370 shows increased global SFe deposition, boosting NPP_{iron} in all Fe-limited regions. The Southern Ocean's increase

is modest (~5%), as rising SH climate-driven fires are balanced by suppressed anthropogenic African fires. The equatorial Pacific sees a ~25% increase, mainly from non-fire SFe sources. Under SSP585, NPP_{iron} decreases in most Fe-limited areas except the North Atlantic, where a mean 17% rise is expected owed to climate-driven North American boreal fires.

The Southern Ocean and high-latitude North Atlantic Ocean are most impacted by climate-driven future fire activity changes, though with differing effects. In the Southern Ocean, reductions in anthropogenic fires and fossil fuel emissions offset climate-driven fire increases, leading to minimal NPP_{iron} change. In contrast, climate-driven fires have a stronger effect on the Fe-limited North Atlantic.

The response of NPP_{iron} in the North Atlantic exhibits pronounced seasonality, with higher relative changes in the NH summer (32% (range, 10–53%) under SSP370 and 44% (range, 30–58%) under SSP585), reflecting the seasonality of boreal fires (Extended Data Fig. 2). This seasonal effect is critical, as Fe limitation in the North Atlantic peaks in the NH summer[36]. The high-latitude North Atlantic exhibits a strong NH spring diatom bloom, producing a substantial seasonal surge of rapidly sinking carbon. Following the spring diatom bloom, extensive coccolithophore blooms persist into late NH summer under Fe-limited conditions[63], contributing to carbon export via sticky exopolymer particles and biominerals[64,65]. Increased NH summer SFe deposition in some scenarios may extend coccolithophore blooms and boost carbon export, aligning with prior studies showing that wildfire aerosol can amplify nitrogen-limited Arctic blooms[8].

Our projections thus far have assumed stable surface nitrate levels, but total NPP changes by century's end will also reflect broader climate impacts. Under low-mitigation scenarios, global warming is expected to increase upper ocean stratification, reducing nutrient mixing from the deep ocean and altering surface macronutrient distribution[66]. This could shrink Fe-limited regions, as shown in CMIP6 projections (Extended Data Fig. 1). When we factor in these macronutrient changes (Methods), NPP_{iron} is projected to decline
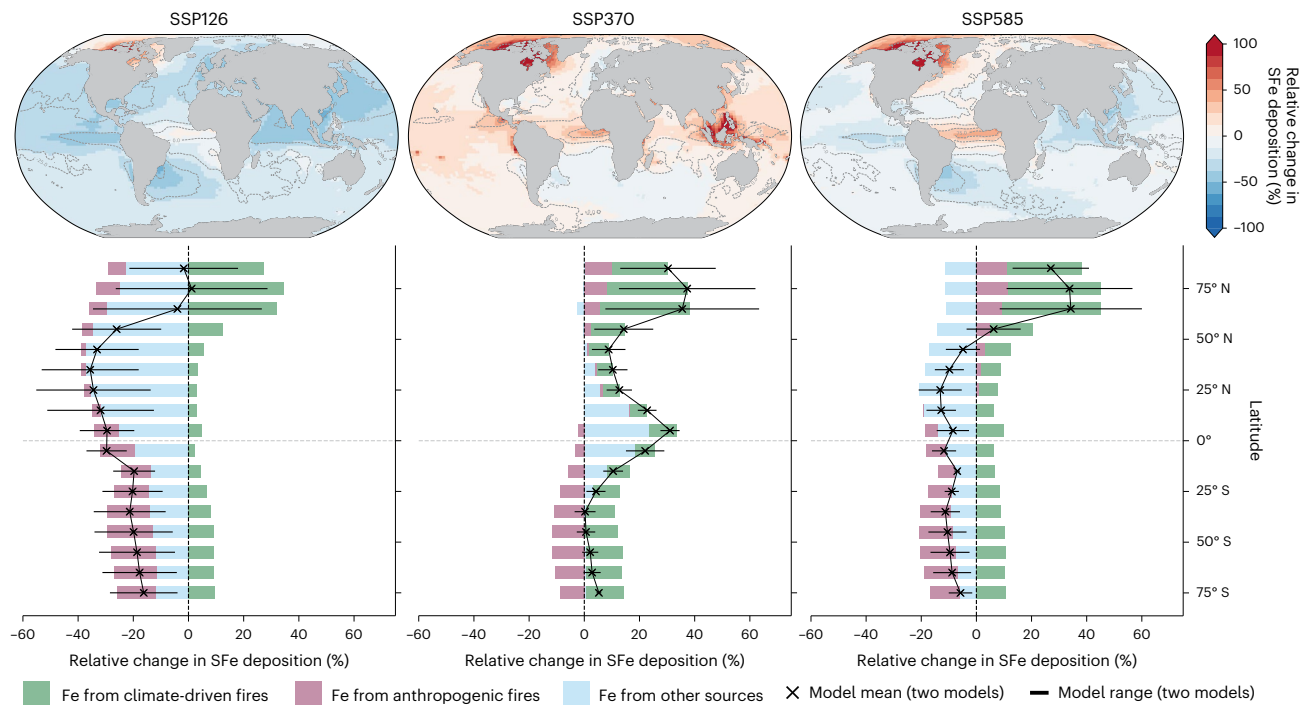
Fig. 3 | Future changes in SFe deposition compared with the present day. Annual mean relative changes in SFe deposition for future scenarios (SSP126, SSP370 and SSP585, from left to right) compared with the present-day scenario. The upper panels show the global distribution of relative changes averaged across two models. The lower panels display the corresponding latitudinal relative changes, where the black crosses indicate the model mean and the bars represent the spread between the two models (CAM6-MIMI and EC-Earth3-Iron). Contributions to the total change from anthropogenic fires (purple), climate-driven fires (green) and other emissions (blue), including dust and fossil fuel sources, are also shown.

across all regions (Extended Data Fig. 1). However, we estimate that climate-driven fires could mitigate this decline, by up to 7–8% in the high-latitude North Atlantic. Additionally, although not considered here or in CMIP6 projections, shifts in fire and other Fe sources will also affect micronutrient-to-macronutrient ratios by influencing not only SFe but also nitrogen deposition (Extended Data Fig. 3). This is particularly noteworthy as stratification may increase the sensitivity of ocean primary production to atmospheric macronutrient inputs, such as those from fire aerosols[8].

These findings are crucial as changes in NPP_{iron}, particularly in the high-latitude North Atlantic, can substantially influence global carbon export and marine ecosystems. Wildfire aerosols may also impact climate by altering albedo and ice sheet melt rates, affecting nutrient availability in high-latitude oceans[67]. Increased wildfires in boreal regions may also enhance nutrient runoff to the ocean, further amplifying these effects[22].

Regional sensitivity to model versus socio-economic uncertainty

Understanding future SFe deposition is crucial for predicting shifts in marine ecosystems and biogeochemical cycles. To understand the drivers of the projections' spread, we calculated the fractional uncertainty across models and scenarios (Fig. 5 and Methods), assessing whether model disparities or different socio-economic scenarios have a greater impact on projected SFe deposition. Regions with low uncertainty show consistent projections regardless of scenario or model differences, while in areas with higher uncertainty we show whether changes are driven mostly by mitigation policies or model variations. This analysis aims to pinpoint key factors influencing SFe deposition, providing insights for both policy and future research.

Our analysis reveals that projected SFe deposition in the NH Fe-limited regions, such as the equatorial and North Pacific and North Atlantic, is mainly driven by socio-economic and climate forcing emission scenarios, including changes in fire emissions. In the North Atlantic, areas near fire sources, such as the Labrador Sea, where SFe deposition strongly increases (Supplementary Fig. 7), exhibit a low fractional uncertainty despite model differences. Fractional uncertainty is considerably higher over other areas of the Fe-limited North Atlantic but decreases markedly in the NH summer when the projected increase in SFe deposition is at its peak, indicating consistency across models and scenarios (Supplementary Fig. 8). Variations in emission policies mainly affect the eastern high-latitude North Atlantic.

In the Fe-limited Southern Ocean, regional differences are evident. In the South American Pyrogenic region (Supplementary Fig. 9) and the SH oceans near Africa, the fractional uncertainty is low, as models and scenarios consistently indicate a slight decrease in SFe deposition. In contrast, in other regions, higher fractional uncertainty arises mainly from model disparities, such as in the South American Dust region (Supplementary Fig. 9), where differences in Fe from dust drive variability. (Supplementary Fig. 10). Model differences also dominate uncertainty in parts of the North Atlantic, South Atlantic, Indian Ocean and Mediterranean.

While projected changes in the Fe-limited North Atlantic are consistent, model differences exist in the magnitude of SFe deposition, with CAM6-MIMI predicting higher deposition than EC-Earth3-Iron (Supplementary Figs. 11 and 6). These discrepancies may partly arise from differences in fire SFe aerosol representation, particularly in fire Fe emission estimates and their global distribution (Methods). EC-Earth3-Iron uses both BC and OC emissions to estimate Fe[29], while CAM6-MIMI relies only on BC[43] (Supplementary Table 1). As a result, the fire Fe emission distribution in EC-Earth3-Iron is mainly driven by the pattern of OC, since OC emissions are higher by mass than BC. In CAM6-MIMI, however, the Fe emission distribution is primarily driven by the BC pattern (Supplementary Fig. 12).

Model differences also arise from how emitted mass is allocated between fine and coarse aerosols. EC-Earth3-Iron assigns
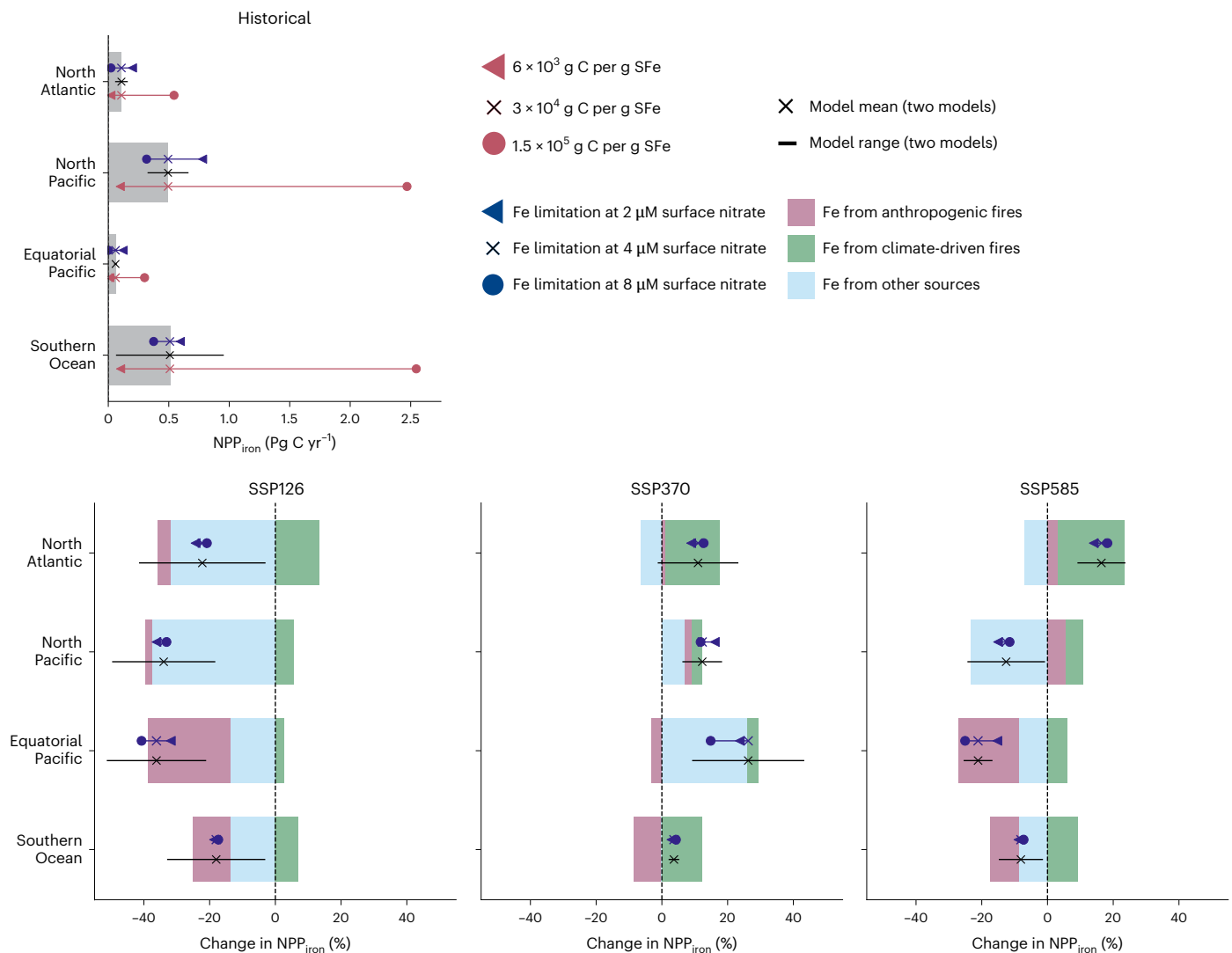
Fig. 4 | Future atmospheric Fe-induced changes in NPP compared with the present. The top panel illustrates the historical model mean (present-day) NPP induced by atmospheric SFe deposition (NPP$_{iron}$) for each Fe-limited region analysed (from top to bottom: North Atlantic, North Pacific, equatorial Pacific and Southern Ocean). The black crosses indicate the model mean, while the black bars represent the range between the two models (CAM6-MIMI and EC-Earth3-Iron). Blue symbols denote results under different nitrate thresholds used to define Fe-limited regions (triangles for 2 μM, crosses for 4 μM and circles for 8 μM). Red symbols show results under a range of C/Fe ratios observed in previous studies (triangles for 6×10^3, crosses for 3×10^4 and circles for 1.5×10^5 g C per g SFe). When one of these parameters (the nitrate limitation threshold or the C/Fe ratio) is changed, the other is set to its central value. The bottom panels illustrate the annual mean relative changes in NPP$_{iron}$ for future scenarios compared with the present-day scenario (SSP126, SSP370 and SSP585, from left to right) accompanied by the relative contributions of changes in anthropogenic fires (depicted in purple), climate-driven fires (depicted in green) and other emissions (depicted in blue).

approximately 22% of the mass to fine particles, while CAM6-MIMI assigns 14%. Coarser particles, with shorter atmospheric lifetimes, lead to more localized SFe deposition in CAM6-MIMI (Supplementary Fig. 13). Additionally, differences in aerosol vertical distribution at emission (Supplementary Table 1) affect spatial deposition patterns, as higher injection heights result in longer transport and particle lifetimes. Disparities in fire Fe dissolution also contribute: CAM6-MIMI assumes 33% and 4% solubility for fine and coarse particles, respectively, while EC-Earth3-Iron emits all fire Fe as insoluble, but with enhanced dissolution during transport (Supplementary Table 1). These differences explain the higher fire Fe solubilities at deposition closer to the boreal fire sources in CAM6-MIMI (Supplementary Fig. 14).

Outlook and future directions

Our study examines the impact of twenty-first-century fire emissions on oceanic SFe supply, considering both climate and anthropogenic

drivers across various socio-economic scenarios. We found that climate change could increase fire-driven Fe emissions by at least 1.7–1.8 times compared with direct anthropogenic drivers of fires alone, with regional variations.

In the NH, particularly under higher-warming scenarios, increased fire emissions lead to a 30–40% rise in SFe deposition. This effect is especially pronounced in the Fe-limited North Atlantic during summer. This increase could boost the effects of SFe deposition on NPP during summer phytoplankton blooms by up to 40%, potentially extending their duration[8] and enhancing carbon export, when assuming present-day macronutrient levels. When accounting for projected declines in macronutrients, climate-driven fires could offset the impact of these declines by 7–8%. In the Southern Ocean, changes in Fe deposition are smaller due to opposing effects from reduced anthropogenic fires, but the region remains sensitive to these shifts, with potential implications for productivity and carbon cycling.
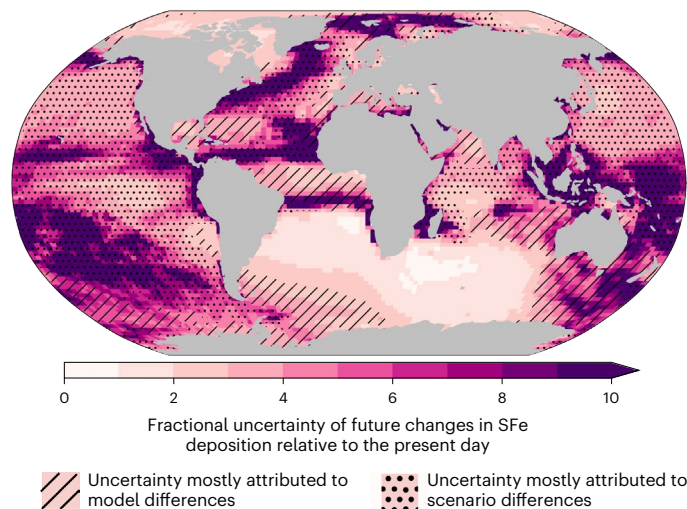
Fig. 5 | Model uncertainty versus socio-economic scenarios. Total estimated fractional uncertainty in SFe deposition changes from the present day to the end of the century, taking into account all scenarios and models. The attribution of uncertainty to model differences and scenario differences is shown with hashed and dotted masks, respectively. Areas without hashed or dotted masks correspond to regions where projected changes across models and scenarios remain statistically similar with a 90% confidence interval after performing a two-tailed *t*-test (Methods).

Uncertainties persist despite our detailed sensitivity analyses, partly due to discrepancies in fire emissions estimates[68–70]. We retained GFED4s present-day estimates to align with the CMIP6 SSP inventory. As GFED4 is on the lower bound of other satellite-based fire emission estimate ranges[68,71], our present-day and future fire Fe emission estimates and associated impacts are probably conservative. Extreme fire events, such as the 2019–2020 Australian megafires, are expected to increase with climate change but are not accounted for in current models, making our projections even more conservative[72].

Model uncertainties also stem from how fire aerosol solubility and vertical distribution are handled, with varying solubility assumptions between models affecting the deposition of fire Fe in different regions[44]. These discrepancies highlight the need for more accurate observational data to refine nutrient emission estimates and improve the representation of fire aerosols in models. This includes the relationship between nutrient content and fire severity, vegetation biome and the type and properties of biomass burning, along with potential shifts between flaming and smouldering in response to a changing climate[29]. Since the model results of SFe deposition are shown to be dependent on these parameters, a multi-model approach, as used here, is essential in such studies.

Fire-driven nutrient supply does not end when a fire ceases, as the removal of vegetation by fire can expose the soil surface, enhancing dust emissions that are also potentially enriched with ash from the fire or modified by its heat[44,73]. Such complex interactions between fire and dust emissions are challenges to tackle in future-generation ESMs.

Additionally, dust emission changes, not considered in this study, could alter SFe deposition in sensitive regions. The North Atlantic and Southern Ocean could be impacted by shifts in dust emissions from regions such as North Africa and East Asia[46]. Given current limitations in dust projections[74], future research should focus on the combined impact of climate- and human-induced changes in both fire and dust emissions.

Our focus in this study is on assessing how future changes in Fe emissions could impact HNLC regions while keeping other factors constant. However, broader climate change factors, such as shifts in meteorological conditions and macronutrient redistribution, also influence biogeochemical dynamics. We show that a warming climate may amplify Fe solubilization and SFe deposition, especially in regions such as the equatorial Pacific, and alter marine productivity through changes in macronutrient distributions and phytoplankton dynamics, further altering the impact of future increases in fires.

Our study motivates detailed ocean biogeochemistry modelling simulations to estimate the overall impact of our refined SFe and nutrient deposition fluxes on ocean biogeochemistry. Climate-driven fires also influence nitrogen deposition, altering Fe:N deposition ratios (Extended Data Fig. 3). This may have an increasingly important effect in HNLC regions under stratification-driven declines in surface nitrate levels and could notably impact nitrogen fixation in other oceanic areas that are depleted in surface nitrate[75]. Moreover, while previous research focused primarily on the fertilization effect of Fe deposition, it is crucial to consider other effects on the ocean biological carbon pump, such as shifts from small phytoplankton to diatoms, potentially enhancing carbon fixation[21]. Expanded observational networks monitoring ocean responses to atmospheric supply, particularly in high-latitude oceans, over the long term should be further supported.

This work exemplifies the trans-disciplinary nature of fire science and the need for a better understanding of fire's role in the oceanic carbon cycle across both spatial and temporal scales. Collaboration among atmospheric science, oceanography and climate policy is crucial to address the challenges posed by shifting fire regimes and their effects on ocean health[76] and to tackle key objectives set by the United Nations Decade of Ocean Science for Sustainable Development[77,78].

Online content

Any methods, additional references, Nature Portfolio reporting summaries, source data, extended data, supplementary information, acknowledgements, peer review information; details of author contributions and competing interests; and statements of data and code availability are available at https://doi.org/10.1038/s41558-025-02356-4.

References

1. Bond, W. J., Woodward, F. I. & Midgley, G. F. The global distribution of ecosystems in a world without fire. *N. Phytol.* **165**, 525–538 (2005).
2. Bowman, D. M. J. S. et al. Fire in the Earth system. *Science* **324**, 481–484 (2009).
3. Voulgarakis, A. & Field, R. D. Fire influences on atmospheric composition, air quality and climate. *Curr. Pollut. Rep.* **1**, 70–81 (2015).
4. Senf, F. et al. How the extreme 2019–2020 Australian wildfires affected global circulation and adjustments. *Atmos. Chem. Phys.* **23**, 8939–8958 (2023).
5. Ball, G., Regier, P., González-Pinzón, R., Reale, J. & Horn, D. V. Wildfires increasingly impact western US fluvial networks. *Nat. Commun.* https://doi.org/10.1038/s41467-021-22747-3 (2021).
6. Byrne, B. et al. Carbon emissions from the 2023 Canadian wildfires. *Nature* https://doi.org/10.1038/s41586-024-07878-z (2024).
7. Pausas, J. G. & Keeley, J. E. Wildfires as an ecosystem service. *Front. Ecol. Environ.* **17**, 289–295 (2019).
8. Ardyna, M. et al. Wildfire aerosol deposition likely amplified a summertime Arctic phytoplankton bloom. *Commun. Earth Environ.* https://doi.org/10.1038/s43247-022-00511-9 (2022).
9. Barkley, A. et al. African biomass burning is a substantial source of phosphorus deposition to the Amazon, tropical Atlantic Ocean, and Southern Ocean. *Proc. Natl Acad. Sci. USA* **116**, 201906091 (2019).
10. Guieu, C., Bonnet, S., Wagener, T. & Loÿe-Pilot, M.-D. Biomass burning as a source of dissolved iron to the open ocean? *Geophys. Res. Lett.* https://doi.org/10.1029/2005GL022962 (2005).

11. Pechony, O. & Shindell, D. T. Driving forces of global wildfires over the past millennium and the forthcoming century. *Proc. Natl Acad. Sci. USA* **107**, 19167–19170 (2010).

12. Bowman, D. M. J. S. et al. The human dimension of fire regimes on Earth. *J. Biogeogr.* **38**, 2223–2236 (2011).

13. Andela, N. et al. A human-driven decline in global burned area. *Science* **356**, 1356–1362 (2017).

14. Jones, M. W. et al. Global and regional trends and drivers of fire under climate change. *Rev. Geophys.* **60**, e2020RG000726 (2022).

15. Westerling, A. L., Hidalgo, H. G., Cayan, D. R. & Swetnam, T. W. Warming and earlier spring increase western U.S. forest wildfire activity. *Science* **313**, 940–943 (2006).

16. Dennison, P. E., Brewer, S. C., Arnold, J. D. & Moritz, M. A. Large wildfire trends in the western United States, 1984–2011. *Geophys. Res. Lett.* **41**, 2928–2933 (2014).

17. Jolly, W. M. et al. Climate-induced variations in global wildfire danger from 1979 to 2013. *Nat. Commun.* **6**, 7537 (2015).

18. United Nations Department of Economic and Social Affairs, Lang, Y. & Moeini-Meybodi, H. *Wildfires—a Growing Concern for Sustainable Development* (UN Department of Economic and Social Affairs, 2021); https://doi.org/10.18356/27081990-111

19. Zheng, B. et al. Increasing forest fire emissions despite the decline in global burned area. *Sci. Adv.* **7**, eabh2646 (2021).

20. McCarty, J. L. et al. Reviews and syntheses: Arctic fire regimes and emissions in the 21st century. *Biogeosciences* **18**, 5053–5083 (2021).

21. Hamilton, D. S. et al. Impact of changes to the atmospheric soluble iron deposition flux on ocean biogeochemical cycles in the Anthropocene. *Glob. Biogeochem. Cycles* https://doi.org/10.1029/2019GB006448 (2020).

22. Riera, R. & Pausas, J. G. Fire ecology in marine systems. *Trends Ecol. Evol.* https://doi.org/10.1016/j.tree.2023.12.001 (2023).

23. Hamilton, D. S. et al. Reassessment of pre-industrial fire emissions strongly affects anthropogenic aerosol forcing. *Nat. Commun.* https://doi.org/10.1038/s41467-018-05592-9 (2018).

24. Li, F. et al. Historical (1700–2012) global multi-model estimates of the fire emissions from the Fire Modeling Intercomparison Project (FireMIP). *Atmos. Chem. Phys.* **19**, 12545–12567 (2019).

25. Tang, W. et al. Widespread phytoplankton blooms triggered by 2019–2020 Australian wildfires. *Nature* **597**, 370–375 (2021).

26. Perron, M. M. et al. Trace elements and nutrients in wildfire plumes to the southeast of Australia. *Atmos. Res.* **270**, 106084 (2022).

27. Wang, Y. et al. Australian fire nourishes ocean phytoplankton bloom. *Sci. Total Environ.* **807**, 150775 (2022).

28. Nguyen, H. D. et al. Effects of dust storm and wildfire events on phytoplankton growth and carbon sequestration in the Tasman Sea, southeast Australia. *Atmosphere* https://doi.org/10.3390/atmos15030337 (2024).

29. Ito, A. Mega fire emissions in Siberia: potential supply of bioavailable iron from forests to the ocean. *Biogeosciences* **8**, 1679–1697 (2011).

30. Ito, A. et al. Pyrogenic iron: the missing link to high iron solubility in aerosols. *Sci. Adv.* https://doi.org/10.1126/sciadv.aau7671 (2019).

31. Paris, R., Desboeufs, K. V., Formenti, P., Nava, S. & Chou, C. Chemical characterisation of iron in dust and biomass burning aerosols during AMMA-SOP0/DABEX: implication for iron solubility. *Atmos. Chem. Phys.* **10**, 4273–4282 (2010).

32. Myriokefalitakis, S. et al. Multiphase processes in the EC-Earth model and their relevance to the atmospheric oxalate, sulfate, and iron cycles. *Geosci. Model Dev.* **15**, 3079–3120 (2022).

33. Ito, A., Ye, Y., Yamamoto, A., Watanabe, M. & Aita, M. N. Responses of ocean biogeochemistry to atmospheric supply of lithogenic and pyrogenic iron-containing aerosols. *Geol. Mag.* **157**, 741–756 (2020).

34. Hamilton, D. S. et al. An aerosol odyssey: navigating nutrient flux changes to marine ecosystems. *Elementa* https://doi.org/10.1525/elementa.2023.00037 (2023).

35. Browning, T. J. & Moore, C. M. Global analysis of ocean phytoplankton nutrient limitation reveals high prevalence of co-limitation. *Nat. Commun.* **14**, 5014 (2023).

36. Ryan-Keogh, T. J. et al. Spatial and temporal development of phytoplankton iron stress in relation to bloom dynamics in the high-latitude North Atlantic Ocean. *Limnol. Oceanogr.* **58**, 533–545 (2013).

37. Baker, C. A., Martin, A. P., Yool, A. & Popova, E. Biological carbon pump sequestration efficiency in the North Atlantic: a leaky or a long-term sink? *Glob. Biogeochem. Cycles* https://doi.org/10.1029/2021GB007286 (2022).

38. Ricour, F., Guidi, L., Gehlen, M., DeVries, T. & Legendre, L. Century-scale carbon sequestration flux throughout the ocean by the biological pump. *Nat. Geosci.* **16**, 1105–1113 (2023).

39. Achterberg, E. P. et al. Iron biogeochemistry in the high latitude North Atlantic Ocean. *Sci. Rep.* https://doi.org/10.1038/s41598-018-19472-1 (2018).

40. Siegel, D. A., Devries, T., Cetinić, I. & Bisson, K. M. Quantifying the ocean's biological pump and its carbon cycle impacts on global scales. *Annu. Rev. Mar. Sci.* **15**, 329–356 (2023).

41. Guivarch, C. et al. in *Climate Change 2022: Mitigation of Climate Change* (eds Shukla, P. R. et al.) 1841–1908 (IPCC, Cambridge Univ. Press, 2023); https://doi.org/10.1017/9781009157926.022

42. Hamilton, D. S. et al. Global warming increases fire emissions but resulting aerosol forcing remains uncertain. Preprint at *Research Square* https://doi.org/10.21203/rs.3.rs-4567012/v1 (2024).

43. Hamilton, D. S. et al. Improved methodologies for Earth system modelling of atmospheric soluble iron and observation comparisons using the Mechanism of Intermediate complexity for Modelling Iron (MIMI v1.0). *Geosci. Model Dev.* https://doi.org/10.5194/gmd-12-3835-2019 (2019).

44. Hamilton, D. S. et al. Earth, wind, fire, and pollution: aerosol nutrient sources and impacts on ocean biogeochemistry. *Annu. Rev. Mar. Sci.* **14**, 303–330 (2022).

45. Randerson, J., van der Werf, G., Giglio, L., Collatz, G. & Kasibhatla, P. *Global Fire Emissions Database, Version 4.1 (GFEDv4)* (ORNL DAAC, 2017); https://doi.org/10.3334/ORNLDAAC/1293

46. Bergas-Massó, E. et al. Pre-industrial, present and future atmospheric soluble iron deposition and the role of aerosol acidity and oxalate under CMIP6 emissions. *Earth's Future* **11**, e2022EF003353 (2023).

47. Archibald, S., Staver, A. C. & Levin, S. A. Evolution of human-driven fire regimes in Africa. *Proc. Natl Acad. Sci. USA* **109**, 847–852 (2012).

48. Janssen, T. A. et al. Extratropical forests increasingly at risk due to lightning fires. *Nat. Geosci.* **16**, 1136–1144 (2023).

49. Hessilt, T. D. et al. Future increases in lightning ignition efficiency and wildfire occurrence expected from drier fuels in boreal forest ecosystems of western North America. *Environ. Res. Lett.* **17**, 054008 (2022).

50. Chen, Y. et al. Future increases in Arctic lightning and fire risk for permafrost carbon. *Nat. Clim. Change* **11**, 404–410 (2021).

51. Jain, P. et al. Drivers and impacts of the record-breaking 2023 wildfire season in Canada. *Nat. Commun.* https://doi.org/10.1038/s41467-024-51154-7 (2024).

52. Rickly, P. S. et al. Emission factors and evolution of SO_2 measured from biomass burning in wildfires and agricultural fires. *Atmos. Chem. Phys.* **22**, 15603–15620 (2022).

53. Zhou, Y. et al. Sources and atmospheric processes impacting oxalate at a suburban coastal site in Hong Kong: insights inferred from 1 year hourly measurements. *J. Geophys. Res. Atmos.* **120**, 9772–9788 (2015).

54. Jones, M. W. et al. Global rise in forest fire emissions linked to climate change in the extratropics. *Science* **386**, eadl5889 (2024).

55. Hamilton, D. S. et al. Recent (1980 to 2015) trends and variability in daily-to-interannual soluble iron deposition from dust, fire, and anthropogenic sources. *Geophys. Res. Lett.* https://doi.org/10.1029/2020GL089688 (2020).

56. Collins, M. et al. Emerging signals of climate change from the equator to the poles: new insights into a warming world. *Front. Sci.* https://doi.org/10.3389/fsci.2024.1340323 (2024).

57. Tebaldi, C. et al. Climate model projections from the Scenario Model Intercomparison Project (ScenarioMIP) of CMIP6. *Earth Syst. Dyn.* **12**, 253–293 (2021).

58. Moore, C. M. et al. Processes and patterns of oceanic nutrient limitation. *Nat. Geosci.* **6**, 701–710 (2013).

59. Boyd, P. W., Arrigo, K. R., Strzepek, R. & Van Dijken, G. L. Mapping phytoplankton iron utilization: insights into Southern Ocean supply mechanisms. *J. Geophys. Res. Oceans* **117**, C06009 (2012).

60. Okin, G. S. et al. Impacts of atmospheric nutrient deposition on marine productivity: roles of nitrogen, phosphorus, and iron. *Glob. Biogeochem. Cycles* **25**, GB2022 (2011).

61. Rathod, S. D. et al. A mineralogy-based anthropogenic combustion-iron emission inventory. *J. Geophys. Res. Atmos.* **125**, e2019JD032114 (2020).

62. Garcia, H. et al. *World Ocean Atlas 2023 Vol. 4: Dissolved Inorganic Nutrients (Phosphate, Nitrate, Silicate)* NOAA Atlas NESDIS 92, p.79 (National Centers for Environmental Information, 2024); https://doi.org/10.25923/39qw-7j08

63. Sanders, R. et al. The biological carbon pump in the North Atlantic. *Prog. Oceanogr.* **129**, 200–218 (2014).

64. Shutler, J. D. et al. Coccolithophore surface distributions in the North Atlantic and their modulation of the air–sea flux of CO_2 from 10 years of satellite Earth observation data. *Biogeosciences* **10**, 2699–2709 (2013).

65. Nissimov, J. I. et al. Dynamics of transparent exopolymer particle production and aggregation during viral infection of the coccolithophore, *Emiliania huxleyi*. *Environ. Microbiol.* **20**, 2880–2897 (2018).

66. Li, G. et al. Increasing ocean stratification over the past half-century. *Nat. Clim. Change* **10**, 1116–1123 (2020).

67. Wadham, J. L. et al. Ice sheets matter for the global carbon cycle. *Nat. Commun.* **10**, 3567 (2019).

68. Liu, T. et al. Diagnosing spatial biases and uncertainties in global fire emissions inventories: Indonesia as regional case study. *Remote Sensing Environ.* **237**, 111557 (2020).

69. Hua, W. et al. Diagnosing uncertainties in global biomass burning emission inventories and their impact on modeled air pollutants. *Atmos. Chem. Phys.* **24**, 6787–6807 (2024).

70. Carter, T. S. et al. How emissions uncertainty influences the distribution and radiative impacts of smoke from fires in North America. *Atmos. Chem. Phys.* **20**, 2073–2097 (2020).

71. Pan, X. et al. Six global biomass burning emission datasets: intercomparison and application in one global aerosol model. *Atmos. Chem. Phys.* **20**, 969–994 (2020).

72. *Spreading Like Wildfire—the Rising Threat of Extraordinary Landscape Fires: A UNEP Rapid Response Assessment* (United Nations Environment Programme, 2022).

73. Yu, Y. & Ginoux, P. Enhanced dust emission following large wildfires due to vegetation disturbance. *Nat. Geosci.* **15**, 878–884 (2022).

74. Kok, J. F. et al. Mineral dust aerosol impacts on global climate and climate change. *Nat. Rev. Earth Environ.* **4**, 71–86 (2023).

75. Duce, R. A. et al. Impacts of atmospheric anthropogenic nitrogen on the open ocean. *Science* **320**, 893–897 (2008).

76. Hamilton, D. S. et al. Igniting progress: outcomes from the FLARE workshop and three challenges for the future of transdisciplinary fire science. *Zenodo* https://doi.org/10.5281/zenodo.12634068 (2024).

77. Muller-Karger, F. E. et al. *Ocean Decade Vision 2030 White Papers—Challenge 2: Protect and Restore Ecosystems and Biodiversity* Ocean Decade Series 51.2 (UNESCO-IOC, 2024); https://doi.org/10.25607/y60m-4329

78. Calewaert, J.-B. et al. *Ocean Decade Vision 2030 White Papers—Challenge 8: Create a Digital Representation of the Ocean* Ocean Decade Series 51.8 (UNESCO-IOC, 2024); https://doi.org/10.25607/bxhy-ra59

Methods

The new future fires dataset

The SSP emission projections from CMIP6 provide a key dataset for studying fire regime changes over the twenty-first century. These SSP scenarios, developed through integrated assessment models, translate socio-economic narratives into spatiotemporally resolved fire emissions under various climate mitigation levels[41]. However, two limitations arise: SSPs exclude the influence of climate change on natural fire activity (that is, climate-driven fire changes), and each SSP relies on different integrated assessment models with diverse assumptions.

In contrast, fire-enabled vegetation models within ESMs simulate how fire regimes respond dynamically to climate factors such as temperature, humidity, precipitation, vegetation distribution and fuel load. Including interactive fire models in this framework enables more accurate predictions of climate-influenced fire behaviour.

A new methodology integrates anthropogenic fire changes from the SSP dataset with climate-driven fire changes from CMIP6 ESM projections to produce monthly emission estimates for each decade throughout the twenty-first century[42]. This approach combines the strengths of both datasets, capturing anthropogenic and climate-driven changes in fire regimes while aligning with present-day satellite-derived estimates.

Anthropogenic fire changes are defined here as those caused by the direct impact of human activities, such as land-use changes, land management and accidents[47]. These are largely influenced by economic and demographic factors[13]. In contrast, climate-driven fire changes are those occurring due to increasingly favourable fire weather conditions, such as low humidity and high temperatures. We acknowledge that changes in these climatic variables, and consequently climate-driven fire changes, are primarily influenced by anthropogenic climate change.

The generation of this emission dataset involved three main steps. First, open-source information from several CMIP6 climate models with interactive fires was collected from https://aims2.llnl.gov/search, hosted on Earth System Grid Federation nodes. In those models, unlike in the SSP inventories, climate change impacts on fire activity are considered. A multi-model mean of fire emissions in each model grid cell was computed using a set of CMIP6 model outputs that incorporate interactive fires: the Community Earth System Model v.2 (CESM2)[79], the CESM2 Whole Atmosphere Community Climate Model (CESM2-WACCM)[79], the Norwegian Earth System Model Medium Atmosphere–Medium Ocean Resolution (NorESM-MM)[80], CNRM-ESM2-1 (ref. 81), the Max Planck Earth System Model v.1.2 Lower Resolution (MPI-ESM1.2-LR)[82] and EC-Earth3-Veg[83]. Among these, three ESMs (CESM2, CESM2-WACCM and NorESM-MM) use the same Community Land Model version 5 (CLM5)[84]. To prevent bias towards CLM5 representation of vegetation and fires, the mean of these three ESMs was initially computed.

Agriculture, deforestation and peat fires were added to the aforementioned ESM output datasets from the SSP datasets[85], as these factors are not considered in the CMIP6 ESMs. However, the SSP dataset does not isolate deforestation fires, which could lead to double counting if added directly. To mitigate this, we assumed that in tropical regions, peat and agricultural fires are predominant, making the SSP estimates for these regions more reliable than those from the CMIP6 ensemble.

Finally, to produce a harmonized dataset with present-day estimates based on observations, each model dataset was bias-corrected towards the present-day (2001–2011) satellite-derived GFED4s dataset[45]. Although we acknowledge the existence of other satellite fire retrievals, we chose GFED4s here as the observational reference, as it is the one used in CMIP6 to estimate present-day fire emissions[85]. Following the approach described in Hamilton et al.[44], the ratio in monthly mean emissions within 20 regions (based on GFED region definitions with additional subdivisions mainly reflecting similarities

in fire behaviour[86]) was calculated between each of the four fire model emission datasets and a GFED4s-derived present-day emission climatology. The regional fire model emission biases were assumed to persist and remain constant through time. We therefore propagated the regional corrections to the ensemble of modelled future fire emissions for each decade in the twenty-first century.

The resulting dataset provides monthly mean carbon (as CO_2) emissions for each decade (in kg C m^{-2} s^{-1} or kg C m^{-2} month^{-1}). To convert to aerosol emissions, we first converted the CO_2 emissions backward to the mass (kg) of biomass burned, assuming 450 g CO_2 emitted per kg biomass burned[87]. We then used the aerosol emission factors per biomass burned (g kg^{-1}) in Andreae[88] to calculate the emission rates of BC, OC, sulfur dioxide and other aerosol species needed for the EC-Earth3-Iron and CAM6-MIMI models.

Emissions for the present day and the last decade of the century were geographically interpolated as required by CAM6-MIMI and EC-Earth3-Iron (Supplementary Table 1).

EC-Earth3-Iron and CAM6-MIMI

ESMs with varying degrees of complexity can be employed to examine the influence of fire aerosols on the deposition of nutrients in the ocean and hence on marine biogeochemistry. To assess how model differences affect estimates of soluble Fe deposition, this study used simulations from two ESMs: EC-Earth3-Iron and CAM6-MIMI. Both models incorporate an atmospheric Fe module encompassing Fe emissions, transport, atmospheric chemistry and both wet and dry deposition. However, they diverge on certain aspects, such as the treatment of oxalate (OXL) formation, which is parameterized[21,89,90] in CAM6-MIMI and explicitly included[32,91] in EC-Earth3-Iron. Further distinctions between the models are summarized in Supplementary Table 1, and brief descriptions of both models are provided hereinafter.

EC-Earth3-Iron builds on the CMIP6 EC-Earth3-AerChem ESM version[92], incorporating a detailed representation of the atmospheric Fe cycle. This included explicit calculation of Fe dissolution in aerosol water and cloud droplets, aqueous-phase OXL formation, and the determination of cloud and aerosol acidity, the latter in both accumulation and coarse modes[32]. An extended evaluation of this configuration is provided in Myriokefalitakis et al.[32]. The EC-Earth3-Iron ESM comprises several modules representing different Earth system components. In this study we used the atmospheric general circulation model, the Integrated Forecasting System from the European Center for Medium-Range Weather Forecasts (ECMWF), coupled to the atmospheric chemistry module, the Tracer Model version 5 release 3.0 (TM5-MP 3.0)[93]. The gas-phase chemistry scheme was resolved through the MOGUNTIA chemical mechanism[94]. SO_4^{2-}, BC, organic aerosols, sea salt and mineral dust microphysics are described by the modal aerosol scheme M7 (ref. 95). Ammonium, nitrate and aerosol water are determined on the basis of gas-particle partitioning. M7 defines seven log-normal modes to represent the aerosols' size distribution and mixing state: four water-soluble modes (nucleation, Aitken, accumulation and coarse) and three insoluble modes (Aitken, accumulation and coarse). Mineral dust emissions are computed online and parameterized according to Tegen et al.[96]. EC-Earth3-Iron TM5 has a horizontal resolution of 3° in longitude by 2° in latitude and 34 vertical layers up to 0.1 hPa.

In EC-Earth3-Iron, Fe emissions from dust and combustion sources (including anthropogenic activities and fires) are taken into account. The emitted dust-Fe (FeD) in the accumulation and coarse insoluble modes is based on a soil mineralogy atlas[97,98], with Fe content estimates for each mineral[99]. Fossil fuel Fe (FeF) and fire Fe emissions are derived by applying specific emission factors to the total carbonaceous particulate emissions (that is, the sum of OC and BC emissions) for each aerosol mode considered and each activity sector[100,101]. The model assumes an initial solubility (that is, the fraction of soluble FeD, SFeD, over total FeD) of 0.1% for all Fe mineral soil

emissions, while combustion emissions are assumed here to be insoluble, except for ship oil combustion. A three-stage kinetic approach is applied to describe the solubilization of the Fe-containing dust mineral pools[102]. A separate Fe pool for combustion aerosols[103] is also considered. The modelled dissolved Fe is produced via dissolution processes in aerosol water and cloud droplets depending on the acidity levels of the solution (that is, the proton-promoted dissolution scheme), the OXL concentration (the ligand-promoted dissolution scheme) and irradiation (the photo-reductive dissolution scheme). The model includes online calculation of aqueous-phase OXL formation, and cloud and aerosol acidity, the latter in both accumulation and coarse modes.

The second model used is the National Center for Atmospheric Research's CESM2 (ref. 79) in its CAM6-MIMI configuration. CAM6-MIMI uses the Community Atmosphere Model v.6 (CAM6) as the atmospheric general circulation model and the Modal Aerosol Module-4 (MAM4)[104]. Mineral dust aerosol is modelled via an updated version of the Dust Entrainment and Deposition model[43,105]. The Mechanism of Intermediate Complexity for Modeling Iron (MIMI)[43] is used to model global atmospheric surface concentrations and deposition fluxes of total and soluble Fe. The model resolution is 1.25° × 0.9375° with 56 hybrid-sigma pressure levels from 1,000 hPa to up to 2 hPa.

Fe emissions from dust and combustion sources (including anthropogenic activities and fires) are also considered in CAM6-MIMI. The emitted FeD in the accumulation and coarse insoluble modes is based on the same soil mineralogical atlas[97] and Fe content estimates for each mineral[106,107]. Fire Fe emissions are derived by applying specific emission factors to the total BC emissions for each aerosol mode, following Hamilton et al.[43]. FeF emissions follow Rathod et al.[61], including coal and smelting, wood, and oil (land and shipping) combustion, with globally uniform soluble fractions at emission of 2%, 10% and 38%, respectively. A two-stage kinetic approach models FeD solubilization, treating the fast-soluble Fe pool as immediately soluble at emission. A separate Fe pool for combustion aerosols is also included. Dissolved Fe forms through proton- and organic-ligand-promoted dissolution. Proton-promoted dissolution depends on estimated [H⁺], calculated from the sulfate-to-calcite ratio and simulated temperature. Organic-ligand dissolution is linked to simulated secondary OC concentrations, as OXL, the primary reactant, is not explicitly modelled.

Present-day simulations show good agreement with the observations of surface concentration of Fe and SFe compiled by Hamilton et al.[44]. The EC-Earth3-Iron and CAM6-MIMI models exhibit strong correlation coefficients (0.69 and 0.70 for total Fe and 0.51 and 0.57 for SFe). Fe concentrations tend to be overestimated in regions heavily influenced by dust sources, such as the North Atlantic and central Pacific. Conversely, in remote areas far from major Fe sources, such as the Southern Ocean downwind of the Patagonian region, there is a noticeable underestimation of Fe concentrations. For more details, see the supplementary material (Supplementary Figs. 15 and 16 and Supplementary Tables 2 and 3).

Simulations

We conducted multiple sets of simulations, each spanning five years, plus a one-year spin-up, using the two models: EC-Earth3-Iron and CAM6-MIMI. These are atmosphere-only simulations, nudged to reanalysis data representing present-day meteorological conditions (2007–2011). EC-Earth3-Iron was nudged using ERA5 reanalysis data from ECMWF[108], while CAM6-MIMI used the MERRA reanalysis[109]. This set-up isolates the effects of different emission scenarios while minimizing the influence of meteorological variability.

The simulations represent two distinct emission periods. The first is the present day (2001–2010), used as a baseline for estimating future changes. The second covers the end of the century (2091–2100) under three CMIP6 SSP scenarios, while meteorological conditions

remain constant at 2007–2011 levels. The three SSP scenarios, SSP126, SSP370 and SSP585, correspond to radiative forcing levels of 2.6, 7.0 and 8.5 W m⁻² by 2100, reflecting diverse socio-economic pathways[110]. SSP1 is denoted as a 'Sustainability' scenario, where the world gradually shifts towards sustainability, prioritizing inclusive development, environmental preservation and reducing inequality through cooperation. SSP3 is a 'Regional rivalry' scenario that assumes weak international cooperation leading to high emissions and barriers to mitigation; the large levels of forcing in SSP370 reflect these difficulties. SSP5 represents a socio-economic future driven by 'Fossil-fuelled development' featuring rapid technological progress and economic growth via competitive markets, innovation and global integration. However, fossil fuel reliance and low environmental concern hinder mitigation in this scenario, resulting in high end-of-century radiative forcing.

To isolate the impact of fire emission changes and more specifically of changes in climate-driven fire emissions by the century's end, three types of simulations were conducted per future scenario and model. One type of simulation used the standard CMIP6 SSP fire emissions (SSP), the second employed the fire emission dataset that also incorporates climate-driven fire changes (SSP$_{wNATFIRES}$) and the third deactivated fire emissions entirely (SSP$_{noFIRES}$). For the present day, two distinct set-ups were implemented: one using GFED4s estimates and one with fires deactivated. In total, 11 atmospheric-nudged simulations were run per model (Supplementary Fig. 2). Given the strong uncertainty in modelled past and future dust trends, for the purpose of this study, dust emissions in all simulations represent present-day levels consistent with meteorological conditions in each model. Non-fire emissions remain constant across each of the three simulations, following CMIP6 SSP data for the corresponding decade and SSP[111]. However, smelting emissions included in CAM6-MIMI were held at present-day levels in future scenarios[61] due to a lack of studies on how these emissions might evolve over time.

Additional sensitivity simulations were conducted using EC-Earth3-Iron, where, instead of nudging the atmosphere towards the reanalysis, the atmosphere was constrained by monthly sea-ice concentrations and sea-surface temperatures, following the Atmospheric Model Intercomparison Project protocol[112]. The monthly sea-ice concentration and sea-surface temperature fields were generated by creating climatologies (2001–2010 for the present day and 2091–2100 for future projections) based on fully coupled EC-Earth3 simulations for each scenario. These outputs are part of the CMIP6 activity and are publicly available. For future projections, all fire emissions (accounting for both anthropogenic and climate-driven changes) were included in this set of sensitivity simulations. Combined with the present-day simulations, this resulted in four simulations (Fig. 2). These simulations estimate how changes in climate affect Fe solubilization, transport and deposition, alongside fire-driven emission shifts.

Source contributions to relative changes

On the basis of the simulation set-up described above, we employed the following methodology to quantify the contributions of changes in climate-driven fires (NATFIRES), anthropogenic-driven fires (ANTFIRES) and fossil fuel emissions and forcing at the end of the century (OTHER) to the future-to-present-day changes in SFe deposition and NPP$_{iron}$. Here RC denotes relative change:

$$RC_{NATFIRES} = 100 \times \frac{SSP_{wNATFIRES} - SSP}{PD} \quad (1)$$

$$RC_{ANTFIRES} = 100 \times \frac{SSP - PD}{PD} - 100 \times \frac{SSP_{noFIRES} - PD_{noFIRES}}{PD} \quad (2)$$

$$RC_{OTHER} = 100 \times \frac{SSP_{noFIRES} - PD_{noFIRES}}{PD} \quad (3)$$

If we sum up the three contributions, we get the total change in SFe or NPP_{iron} at the end of the century compared with the present:

$$RC = 100 \times \frac{SSP_{wNATFIRES} - PD}{PD} \qquad (4)$$

Fe-limited regions

We used surface nitrate concentrations as a proxy for regions sensitive to atmospheric SFe deposition. Fe-limited regions are defined as those where surface nitrate concentrations exceed 4 µM, a threshold supported by both observational and modelling studies[58,113,114]. We also explored threshold values of 2 µM and 8 µM to test the sensitivity of our results to this threshold selection, following previous studies[115].

Present-day Fe-limited regions were identified using surface nitrate concentrations from the World Ocean Atlas 2023[62].

To assess future changes in Fe-limited areas, we analysed nitrate concentrations from seven CMIP6 models that include biogeochemistry with publicly available output: CESM2 (CESM2 and CESM2-WACCM versions), GFDL-ESM4, NorESM2 (NorESM2-LM and NorESM2-MM versions), ACCESS-ESM1-5, MIROC-ES2L, MPI-ESM1-2-LR and UKESM1-0-LL. We calculated ten-year multi-model climatologies for both future (2091–2100) and present-day (2001–2010) periods.

To address model bias, we computed the deviation between modelled present-day climatologies and the observed World Ocean Atlas 2023 fields, and applied this offset to future modelled projections.

Extended Data Fig. 1 (left column) shows the resulting Fe-limited regions. To estimate how model divergence could affect the definition of Fe-limited regions, the same method was applied using the model climatologies adjusted by subtracting and adding the standard deviation of the models (middle and right columns, respectively).

NPP estimates

To estimate NPP_{iron}, we adopted the methodology outlined in Rathod et al.[115]. C/SFe ratios were used in Fe-limited regions. The C/SFe ratios, representing carbon relative to SFe content in phytoplankton biomass or uptake, can vary by several orders of magnitude across different phytoplankton groups and their physiological states. We tested a set of C/SFe ratios (6×10^3, 3×10^4 and 1.5×10^5 g C per g SFe) reflecting the broad range of values reported in the literature[59,60,116,117].

We further accounted for seasonal light changes in high latitudes by excluding from the NPP_{iron} calculations the effects of SFe deposition during November–February in the North Pacific and North Atlantic, and June–September in the Southern Ocean, on the basis of phenology studies[118–122].

Sensitivity assessment

To understand to what extent projected changes in SFe deposition are sensitive to model uncertainty or socio-economic scenario differences, we partitioned the uncertainty[123]. Assuming that both uncertainties are independent, the total uncertainty (T) can be decomposed as follows:

$$T = M + S \qquad (5)$$

where M is the model uncertainty and S is the scenario uncertainty.

We first estimated the model uncertainty for each scenario as the variance of the projected changes between both models. We then used the average across scenarios as the estimate of M:

$$M = \frac{1}{N_s} \sum_s \text{var}_m(x_{m,s}) \qquad (6)$$

where $x_{m,s}$ is the projected change relative to the present day for model m and scenario s, and N_s is the number of scenarios considered (three in our case).

S was calculated as the variance of the multi-model means of projected changes for all scenarios:

$$S = \text{var}_s \left(\frac{1}{N_m} \sum_m (x_{m,s}) \right) \qquad (7)$$

where N_m is the number of models considered (two in our case).

The mean change for all the simulations (G) is the multi-scenario and multi-model mean of the changes:

$$G = \frac{1}{N_m N_s} \sum_{m,s} x_{m,s} \qquad (8)$$

The fractional uncertainty (F) at the 90% confidence level was then calculated as T divided by G, as follows:

$$F = \frac{1.64\sqrt{T}}{G} \qquad (9)$$

We further conducted a two-tailed t-test over the SFe deposition changes to assess statistical significance. P values lower than 0.1 were catalogued as significant, with a 90% confidence level.

Data availability

SFe deposition data for both models (EC-Earth3-Iron and CAM6-MIMI) for each of the scenarios considered are publicly available via Zenodo at https://doi.org/10.5281/zenodo.14961931 (ref. 124). Observational iron data are available from Mahowald et al.[125] and Myriokefalitakis et al.[126], with updates in Hamilton et al.[44]. Data access can be obtained by referring to these publications. Observational data on dust surface concentrations are available from the RSMAS dataset[127] and the AMMA project[128]. CMIP6 Scenario-MIP fire emissions and fire emission projections from ESMs with interactive fires are available via the Earth System Grid Federation archives at https://esgf-node.llnl.gov/search.

Code availability

The EC-Earth3-Iron code is available from the EC-Earth development portal (https://dev.ec-earth.org/) for members of the EC-Earth consortium. Model code developed at ECMWF, such as the Integrated Forecasting System model code, is intellectual property of ECMWF and its member states. Permission to access the EC-Earth3-Iron source code can be requested from the EC-Earth community via the EC-Earth website (http://www.ec-earth.org/) and may be granted if a corresponding software license agreement is signed with ECMWF. The corresponding repository tag is 3.3.2.1-Fe. Due to licence limitations of the model, only European users can be granted access. The model code for CAM6-MIMI is available at http://www.geo.cornell.edu/eas/PeoplePlaces/Faculty/mahowald/dust/Hamiltonetal2019/ (last accessed 17 June 2019). Part of the data processing and analysis in this work used R 4.1.2 (ref. 129), Python 3.7.4 (ref. 130), climate data operators and NetCDF operators. The figure maps were produced using the Python package Cartopy[131], which uses open-source Natural Earth shapefiles.

References

79. Danabasoglu, G. et al. The Community Earth System Model version 2 (CESM2). *J. Adv. Model. Earth Syst.* **12**, e2019MS001916 (2020).

80. Seland, Ø. et al. Overview of the Norwegian Earth System Model (NorESM2) and key climate response of CMIP6 DECK, historical, and scenario simulations. *Geosci. Model Dev.* **13**, 6165–6200 (2020).

81. Séférian, R. et al. Evaluation of CNRM Earth System Model, CNRM-ESM2-1: role of Earth system processes in present-day and future climate. *J. Adv. Model. Earth Syst.* **11**, 4182–4227 (2019).

82. Mauritsen, T. et al. Developments in the MPI-M Earth System Model version 1.2 (MPI-ESM1.2) and its response to increasing CO_2. *J. Adv. Model. Earth Syst.* **11**, 998–1038 (2019).

83. Döscher, R. et al. The EC-Earth3 Earth system model for the Coupled Model Intercomparison Project 6. *Geosci. Model Dev.* **15**, 2973–3020 (2022).

84. Lawrence, D. M. et al. The Community Land Model version 5: description of new features, benchmarking, and impact of forcing uncertainty. *J. Adv. Model. Earth Syst.* **11**, 4245–4287 (2019).

85. van Marle, M. J. E. et al. Historic global biomass burning emissions for CMIP6 (BB4CMIP) based on merging satellite observations with proxies and fire models (1750–2015). *Geosci. Model Dev.* **10**, 3329–3357 (2017).

86. Werf, G. R. V. D. et al. Interannual variability in global biomass burning emissions from 1997 to 2004. *Atmos. Chem. Phys.* **6**, 3423–3441 (2006).

87. Akagi, S. K. et al. Emission factors for open and domestic biomass burning for use in atmospheric models. *Atmos. Chem. Phys.* **11**, 4039–4072 (2011).

88. Andreae, M. O. Emission of trace gases and aerosols from biomass burning—an updated assessment. *Atmos. Chem. Phys.* **19**, 8523–8546 (2019).

89. Johnson, M. S. & Meskhidze, N. Atmospheric dissolved iron deposition to the global oceans: effects of oxalate-promoted Fe dissolution, photochemical redox cycling, and dust mineralogy. *Geosci. Model Dev.* https://doi.org/10.5194/gmd-6-1137-2013 (2013).

90. Scanza, R. A. et al. Atmospheric processing of iron in mineral and combustion aerosols: development of an intermediate-complexity mechanism suitable for Earth system models. *Atmos. Chem. Phys.* **18**, 14175–14196 (2018).

91. Lin, G., Sillman, S., Penner, J. E. & Ito, A. Global modeling of SOA: the use of different mechanisms for aqueous-phase formation. *Atmos. Chem. Phys.* **14**, 5451–5475 (2014).

92. Noije, T. V. et al. EC-Earth3-AerChem: a global climate model with interactive aerosols and atmospheric chemistry participating in CMIP6. *Geosci. Model Dev.* **14**, 5637–5668 (2021).

93. Huijnen, V. et al. The global chemistry transport model TM5: description and evaluation of the tropospheric chemistry version 3.0. *Geosci. Model Dev.* **3**, 445–473 (2010).

94. Myriokefalitakis, S. et al. Description and evaluation of a detailed gas-phase chemistry scheme in the TM5-MP global chemistry transport model (r112). *Geosci. Model Dev.* **13**, 5507–5548 (2020).

95. Vignati, E., Wilson, J. & Stier, P. M7: an efficient size-resolved aerosol microphysics module for large-scale aerosol transport models. *J. Geophys. Res. Atmos.* https://doi.org/10.1029/2003JD004485 (2004).

96. Tegen, I. et al. Impact of vegetation and preferential source areas on global dust aerosol: results from a model study. *J. Geophys. Res. Atmos.* **107**, 4576 (2002).

97. Claquin, T., Schulz, M. & Balkanski, Y. J. Modeling the mineralogy of atmospheric dust sources. *J. Geophys. Res. Atmos.* **104**, 22243–22256 (1999).

98. Nickovic, S., Vukovic, A., Vujadinovic, M., Djurdjevic, V. & Pejanovic, G. Technical note: high-resolution mineralogical database of dust-productive soils for atmospheric dust modeling. *Atmos. Chem. Phys.* **12**, 845–855 (2012).

99. Nickovic, S., Vukovic, A. & Vujadinovic, M. Atmospheric processing of iron carried by mineral dust. *Atmos. Chem. Phys.* **13**, 9169–9181 (2013).

100. Ito, A., Lin, G. & Penner, J. E. Radiative forcing by light-absorbing aerosols of pyrogenetic iron oxides. *Sci. Rep.* **8**, 7347 (2018).

101. Hajima, T. et al. Description of the MIROC-ES2L Earth system model and evaluation of its climate-biogeochemical processes and feedbacks. *Geosci. Model Dev.* https://doi.org/10.5194/gmd-2019-275 (2019).

102. Ito, A. & Shi, Z. Delivery of anthropogenic bioavailable iron from mineral dust and combustion aerosols to the ocean. *Atmos. Chem. Phys.* **16**, 85–99 (2016).

103. Ito, A. Atmospheric processing of combustion aerosols as a source of bioavailable iron. *Environ. Sci. Technol. Lett.* **2**, 70–75 (2015).

104. Liu, X. et al. Description and evaluation of a new four-mode version of the Modal Aerosol Module (MAM4) within version 5.3 of the Community Atmosphere Model. *Geosci. Model Dev.* **9**, 505–522 (2016).

105. Zender, C. S., Bian, H. & Newman, D. Mineral Dust Entrainment and Deposition (DEAD) model: description and 1990s dust climatology. *J. Geophys. Res. Atmos.* https://doi.org/10.1029/2002JD002775 (2003).

106. Journet, E., Desboeufs, K. V., Caquineau, S. & Colin, J. L. Mineralogy as a critical factor of dust iron solubility. *Geophys. Res. Lett.* **35**, 3–7 (2008).

107. Ito, A. & Xu, L. Response of acid mobilization of iron-containing mineral dust to improvement of air quality projected in the future. *Atmos. Chem. Phys.* https://doi.org/10.5194/acp-14-3441-2014 (2014).

108. Hersbach, H. et al. The ERA5 global reanalysis. *Q. J. R. Meteorol. Soc.* **146**, 1999–2049 (2020).

109. Rienecker, M. M. et al. MERRA: NASA's modern-era retrospective analysis for research and applications. *J. Clim.* **24**, 3624–3648 (2011).

110. O'Neill, B. C. et al. The roads ahead: narratives for shared socioeconomic pathways describing world futures in the 21st century. *Glob. Environ. Change* **42**, 169–180 (2017).

111. Hoesly, R. M. et al. Historical (1750–2014) anthropogenic emissions of reactive gases and aerosols from the Community Emissions Data System (CEDS). *Geosci. Model Dev.* https://doi.org/10.5194/gmd-11-369-2018 (2018).

112. Gates, W. L. et al. An overview of the results of the Atmospheric Model Intercomparison Project (AMIP I). *Bull. Am. Meteorol. Soc.* **80**, 29–55 (1999).

113. Krishnamurthy, A., Moore, J. K., Zender, C. S. & Luo, C. Effects of atmospheric inorganic nitrogen deposition on ocean biogeochemistry. *J. Geophys. Res. Biogeosci.* https://doi.org/10.1029/2006JG000334 (2007).

114. Krishnamurthy, A., Moore, J. K., Mahowald, N., Luo, C. & Zender, C. S. Impacts of atmospheric nutrient inputs on marine biogeochemistry. *J. Geophys. Res. Biogeosci.* https://doi.org/10.1029/2009JG001115 (2010).

115. Rathod, S. D. et al. Atmospheric radiative and oceanic biological productivity responses to increasing anthropogenic combustion-iron emission in the 1850–2010 period. *Geophys. Res. Lett.* **49**, e2022GL099323 (2022).

116. Moore, J., Doney, S. C., Glover, D. M. & Fung, I. Y. Iron cycling and nutrient-limitation patterns in surface waters of the world ocean. *Deep Sea Res. 2 Top. Stud. Oceanogr.* **49**, 463–507 (2001).

117. Twining, B. S. & Baines, S. B. The trace metal composition of marine phytoplankton. *Annu. Rev. Mar. Sci.* **5**, 191–215 (2013).

118. Yamaguchi, R. et al. Trophic level decoupling drives future changes in phytoplankton bloom phenology. *Nat. Clim. Change* **12**, 469–476 (2022).

119. Thomalla, S. J., Nicholson, S. A., Ryan-Keogh, T. J. & Smith, M. E. Widespread changes in Southern Ocean phytoplankton blooms linked to climate drivers. *Nat. Clim. Change* **13**, 975–984 (2023).

120. Ardyna, M. et al. Delineating environmental control of phytoplankton biomass and phenology in the Southern Ocean. *Geophys. Res. Lett.* **44**, 5016–5024 (2017).

121. Hieronymus, J. et al. Net primary production annual maxima in the North Atlantic projected to shift in the 21st century. *Biogeosciences* **21**, 2189–2206 (2024).

122. Sasaoka, K., Chiba, S. & Saino, T. Climatic forcing and phytoplankton phenology over the subarctic North Pacific from 1998 to 2006, as observed from ocean color data. *Geophys. Res. Lett.* https://doi.org/10.1029/2011GL048299 (2011).

123. Hawkins, E. & Sutton, R. The potential to narrow uncertainty in regional climate predictions. *Bull. Am. Meteorol. Soc.* **90**, 1095–1107 (2009).

124. Bergas-Masso, E. et al. Data from: Future climate-driven fires may boost ocean productivity in the Fe-limited North Atlantic. *Zenodo* https://doi.org/10.5281/zenodo.14961930 (2025).

125. Mahowald, N. M. et al. Atmospheric iron deposition: global distribution, variability, and human perturbations. *Annu. Rev. Mar. Sci.* **1**, 245–278 (2009).

126. Myriokefalitakis, S. et al. Reviews and syntheses: the GESAMP atmospheric iron deposition model intercomparison study. *Biogeosciences* **15**, 6659–6684 (2018).

127. Prospero, J. M. Long-term measurements of the transport of African mineral dust to the southeastern United States: implications for regional air quality. *J. Geophys. Res.* **104**, 15917–15927 (1999).

128. Marticorena, B. et al. Temporal variability of mineral dust concentrations over West Africa: analyses of a pluriannual monitoring from the AMMA Sahelian dust transect. *Atmos. Chem. Phys.* **10**, 8899–8915 (2010).

129. R Core Team. *R: A Language and Environment for Statistical Computing* (R Foundation for Statistical Computing, 2021); https://www.R-project.org/

130. Van Rossum, G. & Drake, F. L. *Python 3 Reference Manual* (CreateSpace, 2009).

131. Met Office. Cartopy: a cartographic Python library with a Matplotlib interface. http://scitools.org.uk/cartopy (2010–2015).

Author contributions

This study was conceived by E.B.-M., D.S.H., M.G.A. and C.P.G.-P. E.B.-M. wrote the paper with contributions from all co-authors. E.B.-M., with the guidance of D.S.H., produced the needed input with the new fire estimates for the models used here. E.B.-M. set and ran all simulations and analysed the output of EC-Earth3-Iron and CAM6-MIMI. M.G.A. provided scripts for the evaluation of present-day iron concentrations against observations. S.M. contributed with model developments and nitrogen diagnostics. S.R. contributed with model developments. All authors contributed to the interpretation of the results and refinement of the text.

Competing interests

The authors declare no competing interests.

Additional information

Extended data is available for this paper at https://doi.org/10.1038/s41558-025-02356-4.

Supplementary information The online version contains supplementary material available at https://doi.org/10.1038/s41558-025-02356-4.

Correspondence and requests for materials should be addressed to Elisa Bergas-Masso.

Peer review information *Nature Climate Change* thanks Akinori Ito, Rodrigo Riera and the other, anonymous, reviewer(s) for their contribution to the peer review of this work.

Reprints and permissions information is available at www.nature.com/reprints.
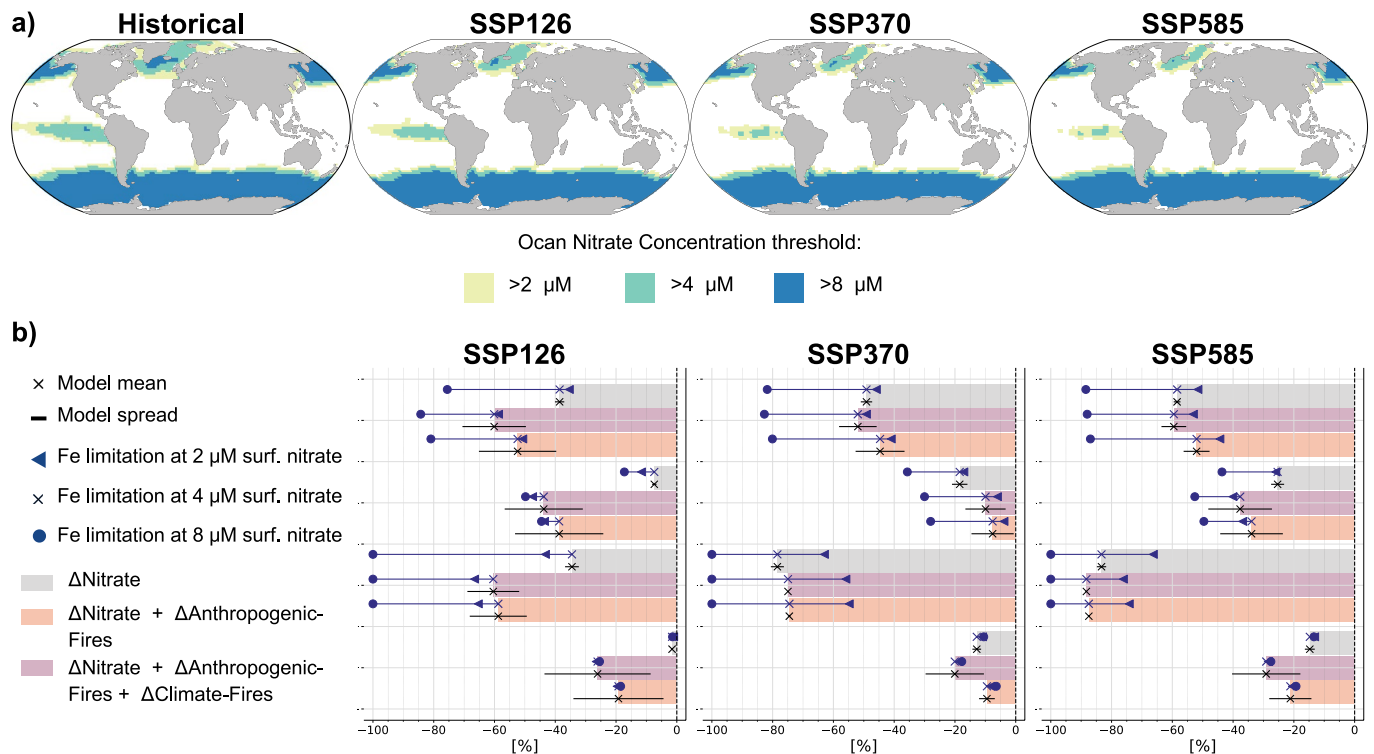
Extended Data Fig. 1 | Changes in Fe limited areas. (a) Ocean surface nitrate concentrations from CMIP6 models for the historical period and future scenarios SSP126, SSP370, and SSP585 (from top to bottom), adjusted to match World Ocean Atlas nitrate concentrations in the historical period. Areas are shown for three different nitrate concentrations thresholds ($2\,\mu M$, $4\,\mu M$, and $8\,\mu M$). **(b)** Impacts of changing Fe-limited areas on future NPP*iron estimates for each scenario (SSP126, SSP370, and SSP585, from left to right) across Fe-limited regions (North Atlantic, North Pacific, Equatorial Pacific, and Southern Ocean, from top to bottom). Grey bars indicate NPP*iron changes when SFe deposition is held constant, accounting only for changes in ocean area limitation. Pink bars show the effects of both area limitation changes and projected anthropogenic SFe sources, while orange bars represent changes when both Fe-limited areas and all SFe sources, including climate-driven fire emissions, are projected to vary. Black crosses show the model mean projected change while black bars depict model range between the two models eployed (CAM6-MIMI and EC-Earth3-Iron). Blue triangles, crosses and circles show the changes when considering different nitrate thresholds to define Fe-limited areas ($2\,\mu M$, $4\,\mu M$, and $8\,\mu M$, respectively).
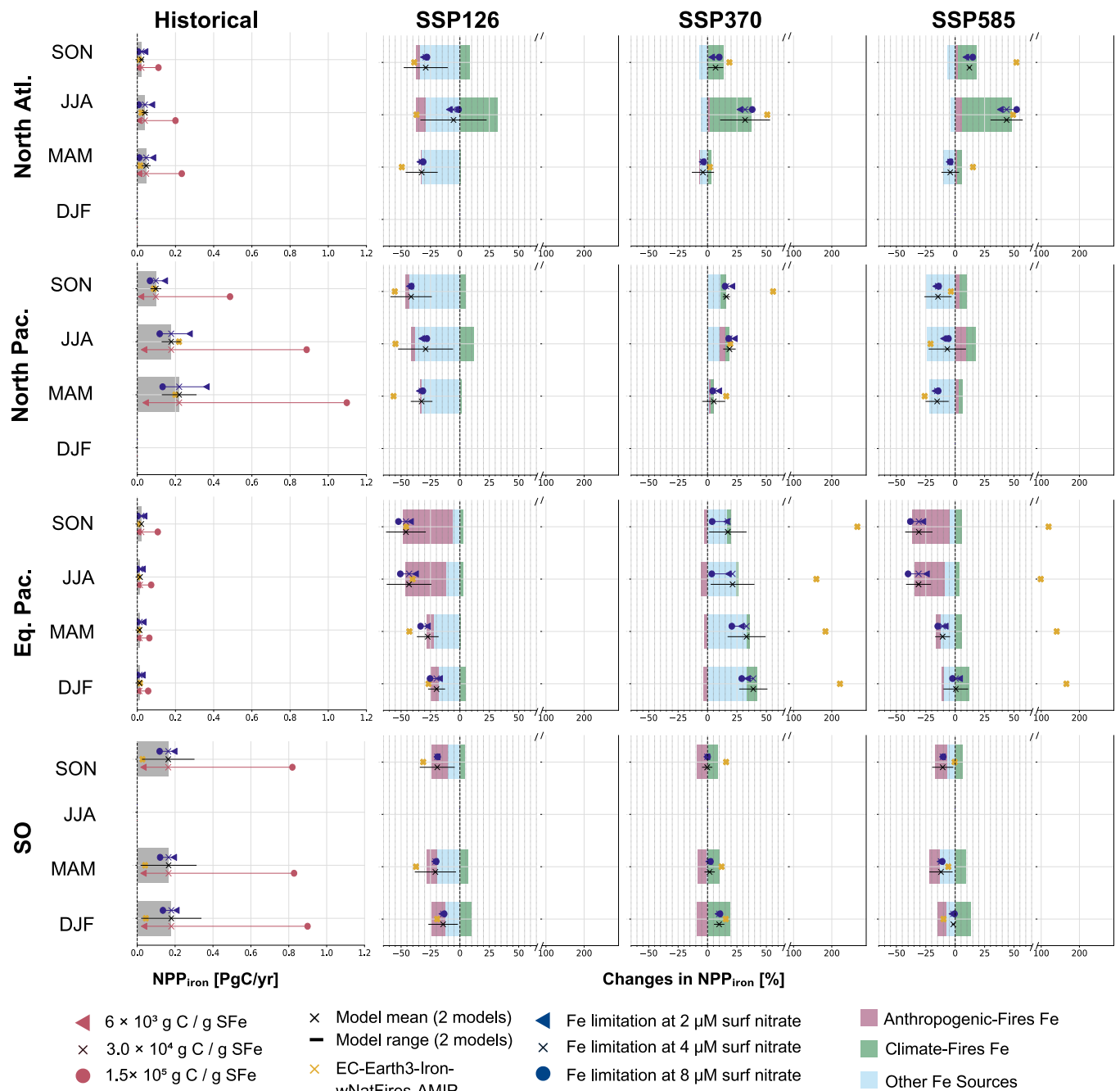
Extended Data Fig. 2 | Future seasonal Fe-induced changes in net primary productivity compared to present. First column shows the historical (present-day) seasonal (SON, JJA, MAM, DJF) net primary productivity induced by SFe deposition (NPP$_{iron}$) for each Fe-limited region analyzed (high-latitude North Atlantic, North Pacific, Equatorial Pacific, Southern Ocean from top to bottom). Second, third and fourth columns show seasonal mean relative changes in NPP$_{iron}$ for future scenarios relative to the present-day scenario (SSP126, SSP370, and SSP585, from left to right) in Fe-limited regions. Regional relative changes are represented by black crosses, accompanied by the contributions to the total change of changes due to anthropogenic fires (depicted in purple), climate-driven fires (depicted in green), and other (depicted in blue). Black crosses show the model mean and black bars represent model range between the two models emplyed (CAM6-MIMI and EC-Earth3-Iron). Red symbols show results under a range of C ratios observed in previous studies (triangle: 6 x 10^3, cross: 3 x 10^4, and circle: 1.4 x 10^5 g C/g SFe). Blue symbols denote results with different nitrate thresholds used to define Fe-limited regions (triangle: 2 μM, cross: 4 μM, and circle: 8 μM). Yellow crosses show the EC-Earth3-Iron-wNatFires-AMIP simulations results.
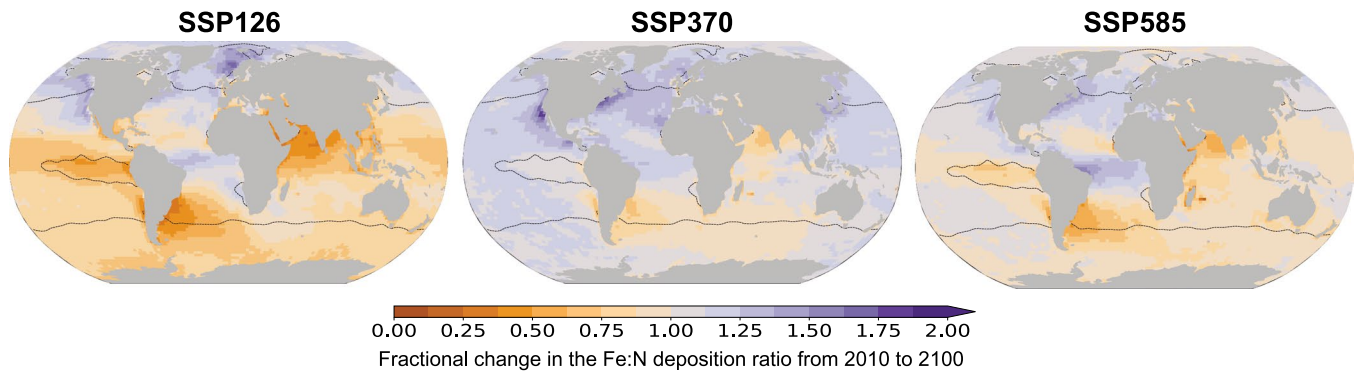
Extended Data Fig. 3 | Fractional change in the Fe:N deposition ratio from 2010 to 2100. Fractional change in the Fe:N deposition ratio from 2010 to 2100 for each scenario (SSP126, SSP370 and SSP585, from left to right) with the new fire dataset.